nature photonics

Article

https://doi.org/10.1038/s41566-023-01332-8

A diamond nanophotonic interface with an optically accessible deterministic electronuclear spin register

In the format provided by the authors and unedited

CONTENTS

I. TAPERED FIBRE FABRICATION

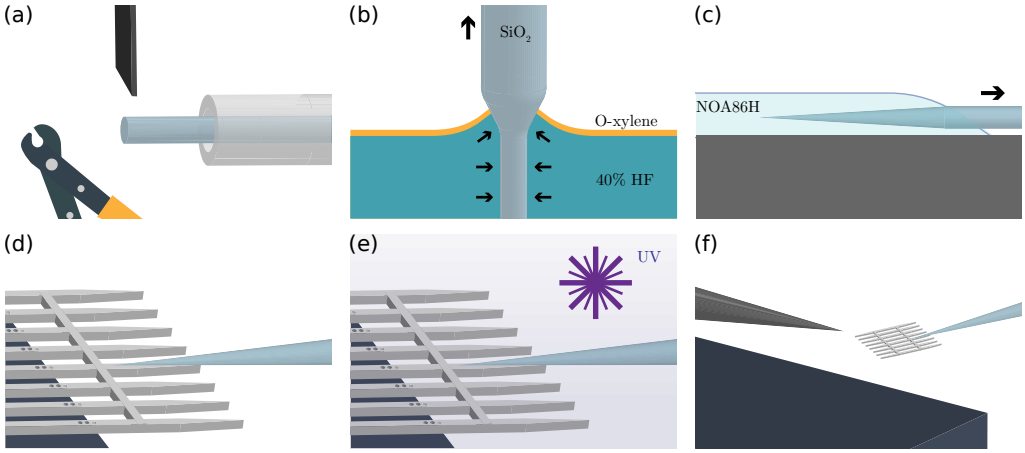

FIG. S1: Schematic description of the photonic packaging process. An optical fibre is (a) stripped and cleaved, (b) inserted and then gradually pulled from a 40% HF solution to form a taper, (c) inserted and removed from an optical adhesive, (d) contacted onto a diamond quantum microchiplet, (e) cured through UV irradiation and, (f) removed from the substrate.

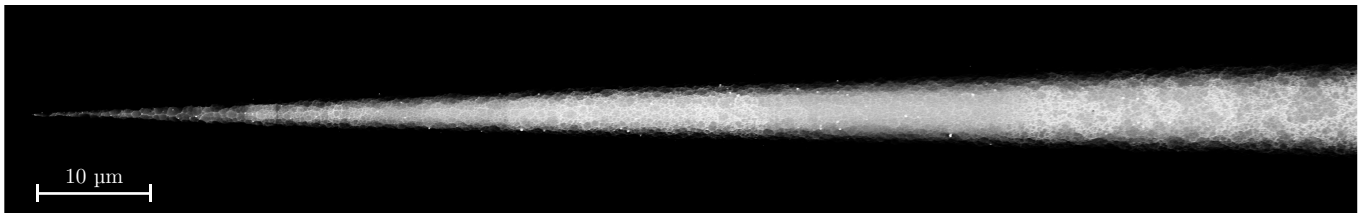

FIG. S2: Adiabatically tapered fibre imaged through Scanning Electron Microscopy (SEM).

Compared to previous work using lensed fibres [1], the change to adiabatically tapered fibres not only greatly enhances the collection efficiency but also enables photonic packaging. The packaging process is illustrated in Fig. S1. A standard single-mode optical fibre (Thorlabs SM600) is first mechanically stripped and cleaved. Adiabatically tapered fibres are then fabricated through dynamic meniscus etching in hydrofluoric acid (HF) [2, 3]. We start with a solution of 80 ml 40% HF and introduce 10 ml of ortho-xylene. Due to their immiscibility, the two liquids separate whereby the lower density ortho-xylene forms a layer at the top of the solution, preventing HF evaporation. A set of fibres is then lowered into the solution and progressively retracted over the course of 95 minutes. We observe an etching rate of 1.5(6) µm/min and thus obtain fibres with a half-angle 1.5(8)° with a pulling rate of 55 µm/min. A characteristic fibre obtained through this process is shown in Fig. S2. A fibre is then coated with a thin layer of a photo-polymerised optical adhesive (Norland Optical Adhesive 86H) [4] by pulling the tapered end of the fibre through a droplet of adhesive. Upon removing the fibre, we visually inspect under an optical microscope that no droplets have formed near the tip of the fibre, indicating that only a thin layer of the adhesive is present. The fibre is then contacted onto the adiabatically tapered port of a diamond waveguide and aligned in a custom-built micromanipulator setup by monitoring the reflection efficiency through the device at 655 nm. A characteristic chiplet device is shown in Fig. S3. The adhesive is then polymerised through UV irradiation at 405 nm with a total irradiation energy density of over 10 Joules cm^{-2}. A tungsten probe is used to remove the chiplet from the substrate edge, forming a packaged device. To obtain optimal adhesion, we anneal the adhesive at 80°C for 3 hours, followed by 50°C for 12 hours. Finally, the device is loaded into the cryostat which is subsequently cooled to ~ 0.4 K, where the sample temperature is monitored by a sensor thermally anchored to the gold-plated copper block affixing the fibre.

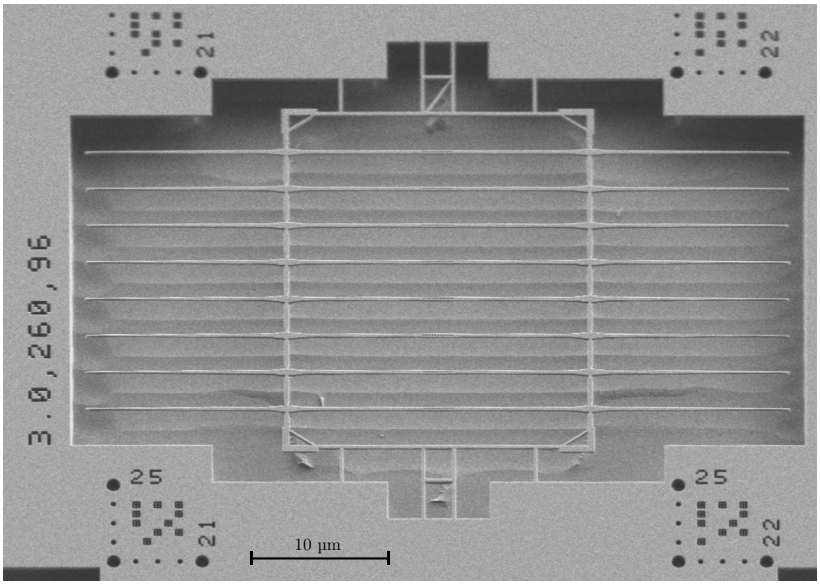

FIG. S3: Scanning Electron Microscopy (SEM) image of a characteristic chiplet device.

II. ANALYSIS OF THE OVERALL DETECTION EFFICIENCY

A. Simulations of waveguide-fibre coupling

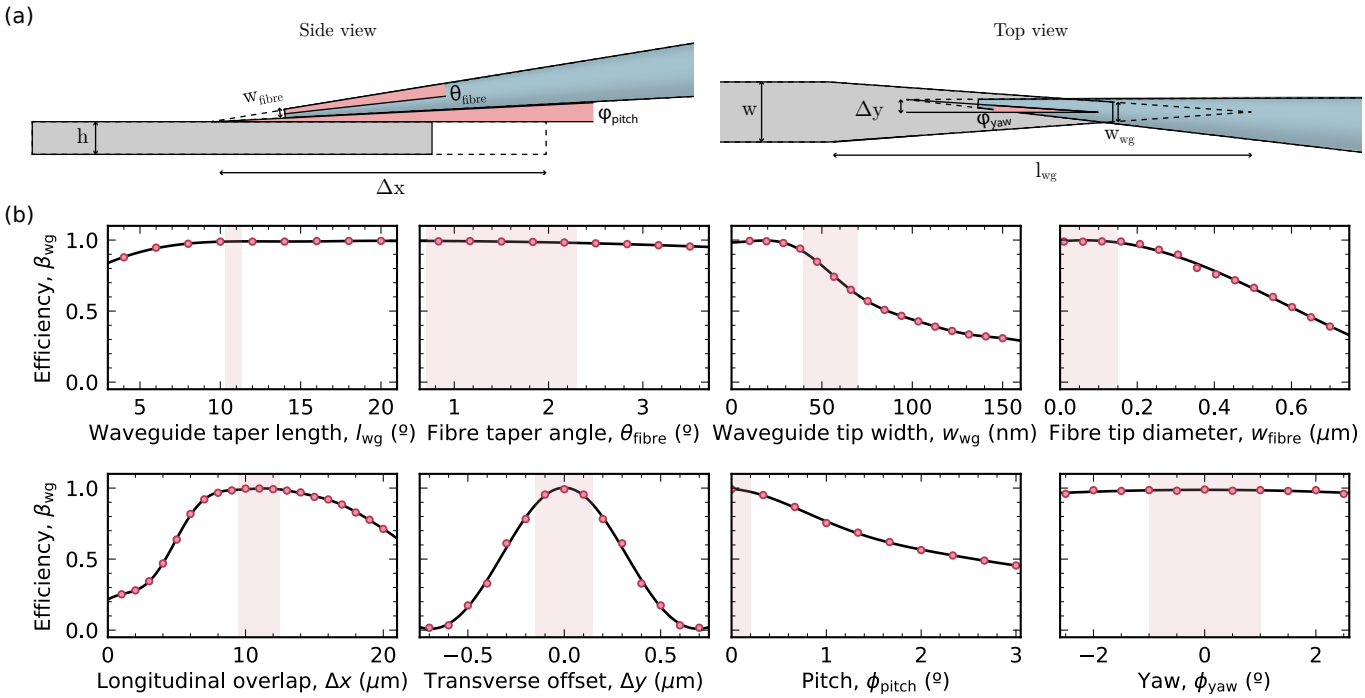

FIG. S4: (a) Diagramatic representation of an imperfect diamond waveguide to fibre alignment. Length dimensions are indicated with arrows whereas angular dimensions are represented with shaded red regions. (b) Coupling efficiency as a function of deviations for each of the parameters in the model. Shaded regions correspond to experimentally realistic ranges for each of the parameters. Solid black lines correspond to smooth fits, based on Gaussian process regression, solely as a guide to the eye.

In this section we numerically evaluate the fibre to waveguide coupling using Finite-Difference Time-Domain

simulations including several realistic alignment and fabrication imperfections. In these simulations the fundamental TE mode of the fibre is excited, and its coupling to the fundamental TE mode of the waveguide is evaluated. Figure S4(a) shows a diagramatic representation of the fibre to waveguide alignment. This is parameterised by the waveguide height (h) and width (w), the waveguide taper length ($l$wg) and fibre tapering angle (θ_{fibre}), the pitch (ϕ_{pitch}) and yaw misalignment (ϕ_{yaw}), the finite diamond tip width (w_{wg}) and fibre tip diameter (w_{fibre}), and the longitudinal overlap (Δx) and transverse misalignment (Δy). In the ideal case $h = 200$ nm, $w = 270$ nm, $l_{\text{wg}} = 11.3$ µm, $\theta_{\text{fibre}} = 1.5°$, $\phi_{\text{pitch}} = 0°$, $\phi_{\text{yaw}} = 0°$, $w_{\text{wg}} = 0$, $w_{\text{fibre}} = 0$, $\Delta x = 0$ and $\Delta y = 12$ µm. For this ideal case, the waveguide to fibre coupling efficiency is higher than 99%.

Figure S4(b) shows how this coupling efficiency varies as fabrication (top row) and alignment (bottom row) imperfections are introduced by perturbing these parameters. The deviation of one parameter can often be compensated by another coupled parameter. For instance, a slight yaw misalignment (ϕ_{yaw}) can be compensated through a small transverse deviation (Δy), or a finite waveguide fibre tip diameter (w_{fibre}) can be compensated by increasing the longitudinal overlap (Δx). In these graphs, the coupling efficiency is thus computed at each point by first optimising the other coupled parameters. As described in SI II-B, we experimentally optimise the alignment by monitoring the reflection before curing the device. As such, it is generally realistic to assume that the maximal point for a given constraint would be found.

Our simulations show that, due to the adiabaticity of the platform, the coupling efficiency is remarkably insensitive to many imperfections. The strong Van der Waals adhesion between the diamond and fibre further ensures that many of the alignment parameters, such as Δy or ϕ_{pitch} are likely very close to the ideal case. The numerical analysis suggests that the limiting factor in the coupling efficiency is the finite width of the diamond tip. This is currently limited by fabrication imperfections in the diamond etching process. From these simulations we estimate that the coupling efficiency should be in the range of 60% - 90%, in reasonable agreement with our experimental reflection measurements.

B. Reflection measurements

We measure the round-trip optical intensity transmission efficiency by injecting a known amount of optical power at 620 nm (quasi-resonant light) into the input port and measuring the reflected intensity back-propagated through the 90:10 beamsplitter, as shown in Fig. 1(b) of the main text. Correcting for the beamsplitter transmission:reflection ratio of 88(1)%:12(1)% at 620 nm, the 0.4 dB excess insertion loss of the beamsplitter and the maximum simulated Bragg reflector efficiency of 95%, we derive a total roundtrip transmission efficiency of 27(3)%, or 52(6)% for a single forward or backward pass. This total transmission efficiency is the product of various losses. To obtain the value for the fibre to waveguide coupling efficiency we correct for the 0.04 dB loss per optical fibre splice, 4% scattering losses from scattering off of the diamond support structure orthogonal to the waveguide's optical axis (as estimated from FDTD), and 12 dB/km Rayleigh scattering losses from our optical fibres (Thorlabs SM600). Correcting for these factors we extract a fibre-waveguide adiabatic mode transfer efficiency of $> 57(6)$%. We highlight that this corresponds to a lower-bound on the adiabatic mode transfer efficiency as the simulated efficiency of the Bragg reflector and the inclusion of no scattering losses due to surface roughness assume an idealised waveguide without fabrication imperfections.

C. Breakdown of the overall detection efficiency

Table S1 presents a breakdown of the factors involved in independently estimating the overall photon detection efficiency. The π-pulse fidelity is characterised through pulsed excitation experiments in SI VI-B. The setup efficiency

Parameter	Description	Efficiency
F_π	π-pulse fidelity	80(1)%
η_{QE}	Quantum efficiency	79(3)% [5]
$1-\eta_{\mathrm{DW}}$	PSB fraction	43(1)% [6]
β_{wg}	Waveguide beta factor	32.5%
η_{fibre}	Waveguide to fibre coupling	57(6)%
η_{setup}	Setup efficiency	51%
η_{det}	Detector efficiency	68%
$\boldsymbol{\eta_{\mathrm{tot}}}$	**Overall detection efficiency**	**$\sim$1.7%**

TABLE S1: Breakdown of the overall detection efficiency.

includes a factor of 79% corresponding to the spectral fraction collected from the phonon sideband. This is a result of only collecting the 638-700 nm region, and is derived from the spectral characterisation in [6]. The estimated overall detection efficiency is in reasonable agreement with the value of 1.40(5)%, extracted from the slope of Fig. 3(c) in the main text.

III. EXTENDED METHODS

A. Setup

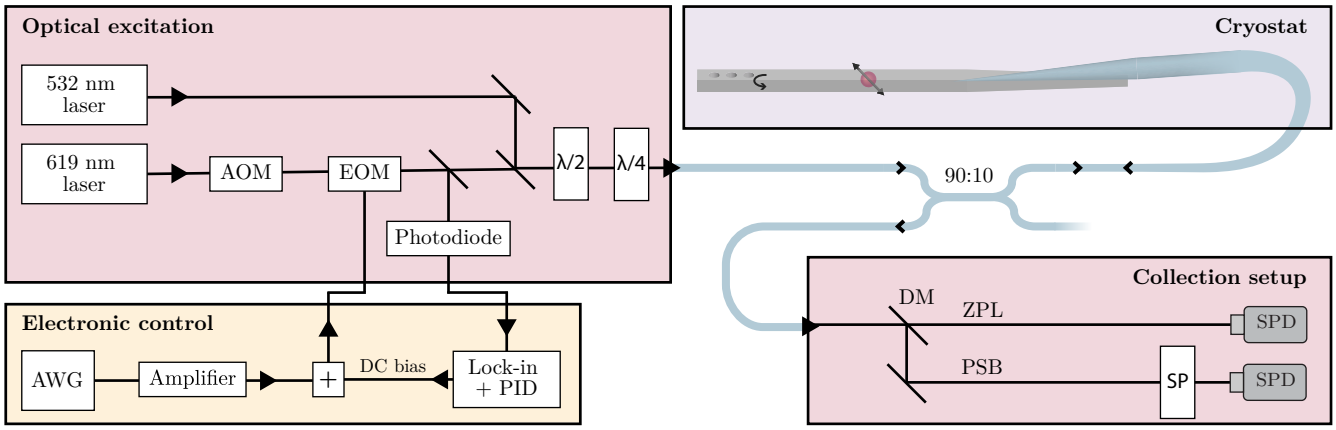

FIG. S5: Schematic of the experimental setup. AOM: Acousto-Optic Modulator. EOM: Electro-Optic Modulator. $\lambda/2$: Half-Wave Plate. $\lambda/4$: Quarter-Wave Plate. DM: Dichroic Mirror. SP: Short-Pass filter. SPD: Single-Photon Detector. AWG: Arbitrary Waveform Generator. The + sign denotes a bias-tee.

Figure S5 shows a schematic of our experimental setup. We employ a tunable resonant source at 619 nm (M2 SolsTiS + EMM) for all of our experiments. The off-resonant source at 532 nm is only employed for measurements of photoluminescence and is not required during on-resonance measurements to initialise the charge state of the emitter [7]. The resonant light is directed through an acousto-optic modulator (AOM, Gooch and Housego 3080-15) and a fibre-based electro-optic modulator (EOM, Jenoptik AM635). The EOM is used for all optical pulsing and is controlled by a 25 Gsamples/s arbitrary waveform generator (Tektronix AWG70002A) through a microwave amplifier (Minicircuits ZX60-83LN12+) and a bias-tee (Minicircuits ZFBT-6G+). The resonant laser is detuned by 3.5 GHz from the middle point of the C1 and C2 transitions to minimise the laser excitation caused by leakage laser light, and near-resonant light is generated through sinusoidal modulation of the EOM with a frequency swept around 3.5 GHz.

In all resonant measurements the EOM is stabilised to its interferometric minimum through a lock-in amplifier and PID loop (Red Pitaya, STEMlab 125-10). A pulse generator (Swabian Instruments Pulse Streamer 8/2) is employed as a master clock to coordinate all instruments.

After modulation and polarisation control, the light is routed via a 90:10 fibre based beamsplitter (Thorlabs broadband custom SM600 90:10 beampslitter), to the tapered SM600 fibre inside the cryostat (Bluefors LD250 He dilution refrigerator at 120 mK). Connections between SM600 fibres are spliced to minimise insertion losses. Vacuum is maintained inside the cryostat by an epoxy seal (Loctite Ablestick 285, 24LV catalyst) hardened after threading the fibre through a custom feedthrough.

The light emitted by the SnV centre is separated into phonon sideband (PSB) and zero phonon line (ZPL) components by a dichroic mirror (Thorlabs DMLP638) with a tunable long-pass filter employed for further suppression of the resonant light in the PSB path (Semrock BLP01-633R-25). A shortpass filter FESH0700 is also employed in the PSB path. All detection is performed by fibre-coupled single photon detectors (Excelitas SPCM-AQRH-16-FC). In Fig. 4 of the main text neutral density filters (Thorlabs NE20A and NE03A) are employed to reduce the photon flux at the ZPL single-photon detector.

B. Data acquisition and analysis

In Fig. 2(c) and Fig. 3(b) of the main text, optimal initialisation via the C1 and C2 transitions was achieved when the frequency of the optical pump was blue-detuned or red-detuned by ~ 40 MHz respectively, that is when the laser frequency is closer to the centre of the two transitions. Similarly, optimal readout was achieved when the frequency of the optical probe was detuned by ~ 40 MHz, in this case away from the centre of the two transitions. A possible explanation for this effect is a splitting due to hyperfine coupling in the excited state that results in split nuclear-conserving and nuclear-flipping transitions to the excited state.

All the ^{117}SnV centres investigated in this work show a bi-stable emission behaviour between a bright and a dark state. This phenomenon has been consistently observed across multiple independent studies of SnV centres [1, 6, 8] and has been postulated to be due to a charge-state instability [7]. In this work this manifests as a $\sim 40\%$ duty-cycle for the bright-state of the ^{117}SnV. The overall detection efficiency presented in the main text enables single-shot identification of this state based on the timetrace of the fluorescence. Accordingly, the data presented in Fig. 2(c-d), Fig. 3(a-b) and Fig. 4 is post-selected for when the ^{117}SnV centre is in the bright-state. We do not post-select Fig. 3(c), to show the true probability of detection in a 24 h period. In Fig. 4, to correct the power fluctuations in the excitation intensity as the EOM sideband is scanned over the transition, we take a reference measurement off-resonant from the emitter and use it to normalise the reflection data. Additionally, as the EOM generates positive and negative sidebands of equal intensity, but only one of them is being scanned through the emitter resonance, we correct the data for a 50% background.

C. CORE vs. PLE measurements for isotope spectroscopy

Figure S6 highlights the difference between PLE an CORE in signal purity on ^{117}SnV colour centres. When PLE measurements are taken, the resonant laser is scanned across the transition slower than the optical initialisation rate (top Fig. S6). At low powers, this optical pumping terminates the fluorescence and no signal is detected. At high powers, $s \gg 1$, power broadening of the transitions prevents optical pumping but also impedes resolving the hyperfine structure. When a CORE scan is conducted (bottom Fig. S6) a clear signal is seen, as minimal optical pumping takes place even at $s \ll 1$.

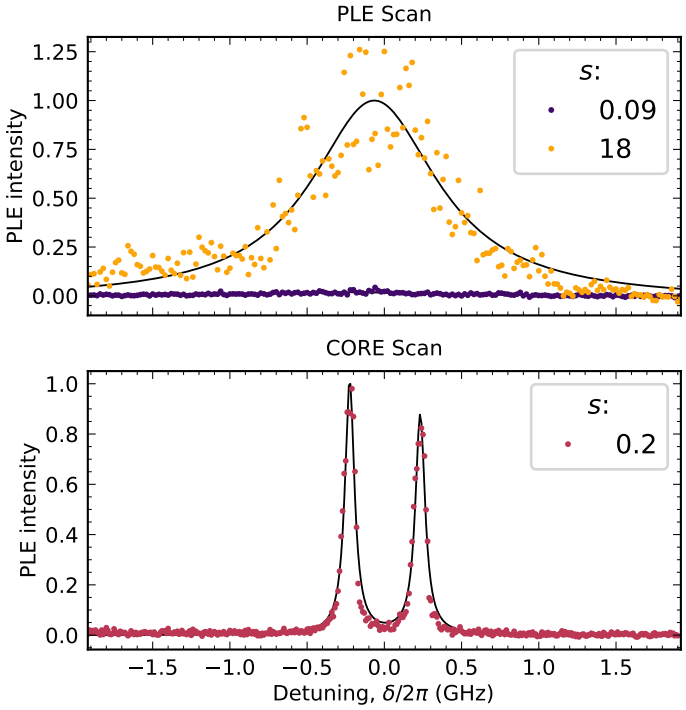

FIG. S6: The variation in photoluminescence excitation (PLE) intensity as a resonant laser is scanned across the transition is shown. The legend lists the saturation parameter (s) used for each scan. The top sub-figure highlights the spectral response when a traditional scan is performed, with scan rate less than the optical initialisation rate. The bottom sub-figure highlights the spectral response for a CORE scan.

IV. ELECTRO-NUCLEAR HAMILTONIAN

A. Theoretical description

We consider the electronuclear Hamiltonian of the ground state

$$H = \underbrace{\lambda L_z S_z}_{H_{\mathrm{SO}}} + \underbrace{\gamma_S \boldsymbol{B}\cdot\boldsymbol{S}}_{H_{\mathrm{Zeeman,S}}} + \underbrace{\gamma_I \boldsymbol{B}\cdot\boldsymbol{I}}_{H_{\mathrm{Zeeman,I}}} + \underbrace{A_\parallel S_z I_z + A_\perp (S_x I_x + S_y I_y)}_{H_{\mathrm{hf}}}, \tag{1}$$

where $\lambda/2\pi = 850$ GHz [9] is the spin-orbit coupling constant, $\gamma_S/2\pi = 28$ GHz/T the electron gyromagnetic ratio, $\gamma_I/2\pi = -15.24$ MHz/T is the nuclear gyromagnetic ratio for ^{117}Sn and $A_\parallel$ and $A_\perp$ are the parallel and perpendicular hyperfine coupling constants respectively. The angular momentum operators can explicitely be written in the $|e_{g+}\rangle$, $|e_{g-}\rangle$ orbital basis [10] by $L_z = \sigma_z$, $\boldsymbol{S} = \boldsymbol{\sigma}/2$, $\boldsymbol{I} = \boldsymbol{\sigma}/2$, where $\boldsymbol{\sigma} = (\sigma_x, \sigma_y, \sigma_z)$ is a vector containing the three Pauli matrices. This includes the dominant effects of spin-orbit coupling and electronic Zeeman effect for the electron; the nuclear Zeeman effect for the nucleus; and the hyperfine interaction between the two. We do not include the effects of strain, Jahn-Teller, and the orbital Zeeman effect in this discussion.

At zero-magnetic field and with no hyperfine interaction present, the eigenstates of the Hamiltonian are split into two branches, with energies $\pm\lambda/2$. In the lower branch, which forms the ground state, the eigenvectors are $|e_+ \downarrow\rangle$ and $|e_- \uparrow\rangle$. Notably, this implies that even at $\boldsymbol{B} = \boldsymbol{0}$, spin-orbit constrains the electron spin to be aligned to the symmetry axis of the defect, z. When an off-axis magnetic field is applied (B_x, B_y), it results in a competition between the magnetic and spin-orbit quantisation axes and thus only in a negligible quadratic energy shift. A magnetic field along

the z axis, on the contrary, results in a linear splitting at a rate $\pm\gamma_S B_z$. For this reason, the hamiltonian is often reduced for just the two ground state levels to include an anisotropic g-factor $H_{\text{Zeeman,S}} \rightarrow \gamma_S B_z S_z$.

The addition of a hyperfine interaction results in a similar quantisation axis competition for the nuclear spin. The lower angular branch of the ground state consists of two levels, each doubly degenerate, with energies given by,

$$E_{\uparrow\Uparrow,\downarrow\Downarrow} = -\frac{\lambda}{2} + \frac{A_\parallel}{4}, \quad E_{\uparrow\Downarrow,\downarrow\Uparrow} = -\frac{\sqrt{\lambda^2 + A_\perp^2}}{2} - \frac{A_\parallel}{4} \approx -\frac{\lambda}{2} - \frac{A_\parallel}{4} \tag{2}$$

where $E_{\uparrow\Uparrow,\downarrow\Downarrow}$ and $E_{\uparrow\Downarrow,\downarrow\Uparrow}$ refer respectively to the energy of the states with aligned and anti-aligned electron and nuclear spins. To first order, only the parallel component of the hyperfine coupling affects the eigenenergies. The strong spin-orbit coupling which resulted in a pinning of the quantisation axis of the electron now results, via the electron, in a pinning of the quantisation axis of the nucleus. When a magnetic field is applied along B_z, the eigenstate splitting is given by $\pm\gamma_S B_z \pm \gamma_N B_z$. The reduced Hamiltonian for the lower orbital branch of the ground state can thus be written in the form

$$H \approx \gamma_S^* B_z S_z + \gamma_I B_z I_z + A_\parallel S_z I_z, \tag{3}$$

where γ_S^* is now an effective gyromagnetic ratio that now includes the effects of the orbital Zeeman effect [10]. We note that $\gamma_I B_z \ll A_\parallel$ for all realistic magnetic fields probed in this work and thus the nuclear gyromagnetic ratio γ_I can be neglected in most cases.

B. Magnetic field splitting

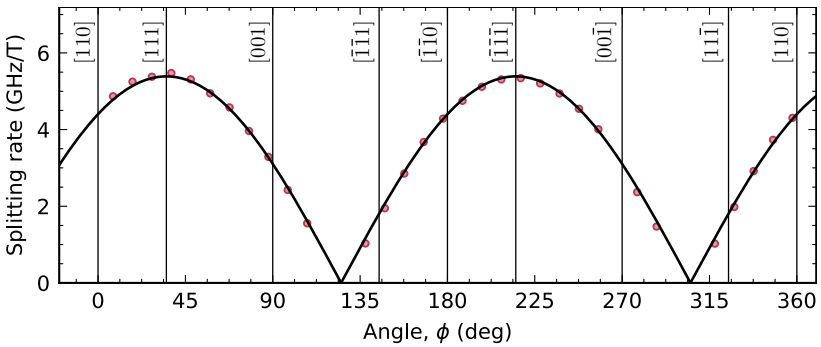

FIG. S7: Splitting rate of the two spin conserving transitions derived from Lorentzian fits to CORE scans while the magnetic field is scanned in a plane orthogonal to the [$\bar{1}$10] crystallographic axis at a fixed magnitude of 50 mT. The solid black line is a fit to $|A\cos(\phi + \phi_0)|$, with free fit parameters A and ϕ_0.

Figure S7 shows the splitting rate of the two spin conserving transitions seen in PLE as a function of the magnetic field orientation. The magnetic field is scanned in a plane orthogonal to the [$\bar{1}$10] crystallographic axis. A magnetic field parallel to the axis of the emitter is expected to lead to a first-order splitting, while a perpendicular field is expected to lead to no first-order splitting. We thus extract that the symmetry axis of the emitter studied in this work is the [111] axis. In Fig. 2(a) of the main text the magnetic field was scanned along the [110] axis. We thus extract B_z, the magnetic field along the emitter axis, through a factor of $\cos(35°)$

C. PLE of multiple emitters

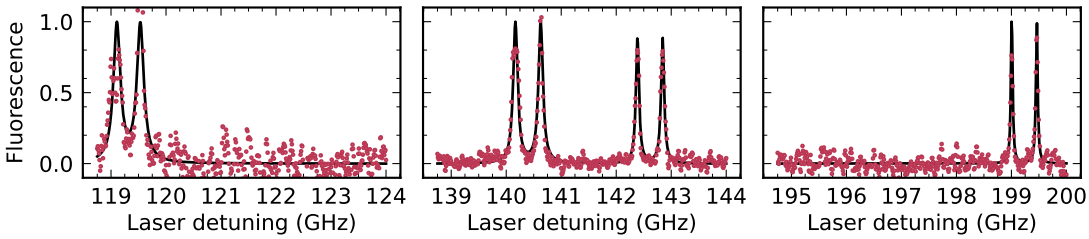

FIG. S8: A characteristic selection of CORE scans across multiple ^{117}SnV centres, with laser frequency measured from the relative detuning to 484.000 THz. (left) The ^{117}SnV centre at the minimum of the inhomogeneous distribution. (middle) Two ^{117}SnV centres near the centre of the inhomogeneous distribution. (right) The ^{117}SnV centre at the maximum of the inhomogeneous distribution.

A characteristic selection of CORE scans across distinct emitters is shown in Fig. S8. The inhomogeneous strain in the device results in an inhomogeneous spectral distribution of ^{117}SnV centres. Accordingly, we find distinct emitters located in a $\sim$85 GHz spectral range from 484.115 THz to 484.200 THz. Figure S8 shows PLE scans of SnV centres sampled from the tails and the centre of the inhomogeneous distribution. In all cases, the same optically resolvable hyperfine splitting is observed.

V. SUPPLEMENTARY EMITTER CHARACTERISATION

A. Lifetime measurement

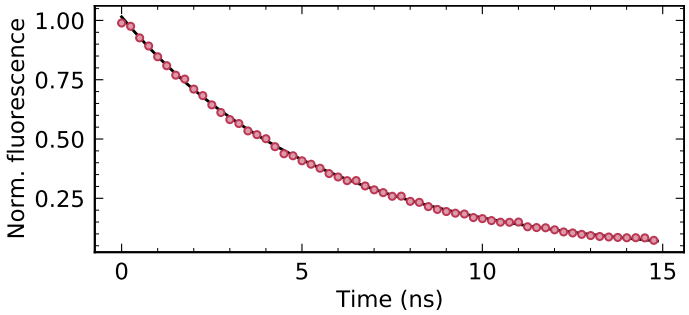

FIG. S9: PSB fluorescence decay following an optical π-pulse. The fit is to a single exponential function with decay constant $\tau_{\mathrm{sp}} = 5.56(3)$ ns.

Measurements of the lifetime are presented in Fig. S9, obtained by applying a π-pulse to the excited state and collecting the subsequent decay. This yields a single-exponential decay with lifetime $\tau_{\mathrm{sp}} = 5.56(3)$ ns or equivalently a Fourier limit of $\gamma_0/2\pi = 28.6(1)$ MHz.

B. Optical π-pulse characterisation

To measure the photon detection events in Fig. 3c of the main text, the ^{117} SnV was initialised into the $|1\rangle$ state and subsequently excited with a train of optical π-pulses with a separation of 100 ns. Figure S10 shows Rabi oscillations of the excited state population from applying a pulse on resonance with the C1 transition at $t = 0$. A π-pulse is achieved in 1.8(1) ns with 80(1)% fidelity. The fit to the excited state population (ρ_{ee}) is of the form [11]:

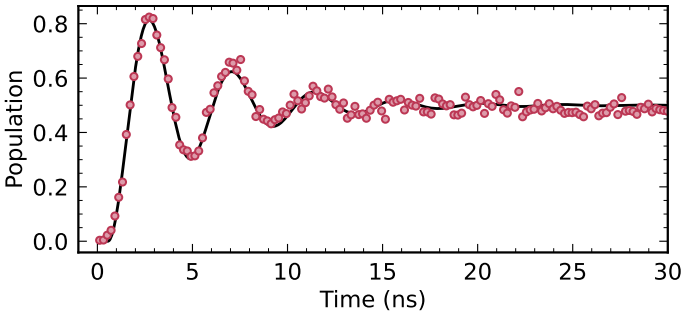

FIG. S10: Optical Rabi oscillations between the ground and excited-state manifolds.

$$\rho_{\mathrm{ee}} = \frac{1}{2}[1 - \{\cos(\Omega t) + \frac{1}{\Omega T_1}\sin(\Omega t)\}e^{-t/T_1}], \tag{4}$$

where $T_1 = 4.7(2)$ ns is the optical relaxation time, $\Omega = 2\pi \cdot 230(10)$ MHz the Rabi rate and t the resonant drive time, where the steady-state population has been normalised to 0.5 at long drive times ($t > 30$ ns). The π-pulse fidelity is given by the maximum population achieved in the excited state

VI. THEORY OF OPTICAL NONLINEARITY

In this section, we describe the theoretical reflection spectrum of our waveguide device and its dependence on the cooperativity. Based on the measured cooperativity and other parameters, we estimate a lower bound on the quantum efficiency.

For a cavity resonantly coupled to a two-level emitter (TLE), the reflected amplitude of light in near resonance with the TLE is given by [12, 13]

$$r(\delta) = 1 - \frac{2\kappa_{\mathrm{in}}/\kappa_{\mathrm{tot}}}{1 + C/(1 + 2\mathrm{i}\delta/\gamma_{\mathrm{h}})}, \tag{5}$$

where C is the cooperativity of the light-matter interface, γ_{h} is the homogeneous linewidth of the emitter in the absence of Purcell enhancement, and δ is the detuning of the incident light from the TLE. κ_{tot} is the total decay rate of the cavity and κ_{in} is the decay rate into the input port of the cavity, which in our case is towards the adiabatically tapered fibre. For compactness, we define the ratio $f = \kappa_{\mathrm{in}}/\kappa_{\mathrm{tot}}$ which is ideally unity. To apply the cavity formalism to a Bragg reflector yielding constructive interference, we have assumed the case of a highly broadband cavity ($\kappa_{\mathrm{tot}} \gg \gamma_{\mathrm{h}}$), which ensures near-perfect resonance between the cavity and the TLE. Additionally, we assume that the TLE is driven well below saturation.

In the experiment, we report the reflection intensity normalised to the far-detuned reflection intensity

$$\mathcal{R}(\delta)_{norm} = \frac{|r(\delta)|^2}{|r(\delta \gg \gamma_h)|^2}. \tag{6}$$

Of particular interest is the normalised reflection at zero detuning

$$\mathcal{R}(\delta = 0)_{norm} = \frac{|r(\delta = 0)|^2}{|r(\delta \gg \gamma_h)|^2} = \left(\frac{1 - 2f/(1 + C)}{1 - 2f}\right)^2 \tag{7}$$

where the cooperativity is given by $C = \Gamma/\gamma_h$, where Γ is the rate of ZPL emission via the C-transition into the cavity mode. Γ can be related to the total emitter decay rate γ_0 via

$$\Gamma = \underbrace{\beta_{cav} \times \eta_{DW} \times \eta_{QE} \times \eta_{orb}}_{\beta_{tot}} \times \gamma_0, \tag{8}$$

where β_{cav} is a photonic property representing the fraction of photons emitted into the cavity mode, η_{DW} is the Debye-Waller factor representing the fraction of photons emitted into the ZPL, η_{QE} is the quantum efficiency and η_{orb} is the orbital branching ratio.

Using Eq. 6, we fit the results in Fig. 4 of the main text, giving a cooperativity of $C = 0.027(3)$. This is the average value extracted from the fits of the two transitions in Fig. 4(b) after correcting for the finite initialisation fidelity of the state. This slightly reduced initialisation fidelity, relative to the high fidelity realised after 30 μs of pumping in Fig. 2(c) of the main text, is chosen to increase the repetition rate of the experiment. We additionally constrain $f = 0.95$ based on numerical simulations of the Braff reflectors.

Equation 8 then allows us to estimate η_{QE} from the values of γ_h, β_{cav}, η_{DW}, η_{orb} and γ_0. From PLE scans we extract a homogenous linewidth of $\gamma_h = 70(5)$ MHz. The measured radiative lifetime $1/\gamma_0 = 5.56(3)$ ns only deviates slightly from the value measured in bulk [5] implying negligible Purcell enhancement, and we thus assume that the measured homogenous linewidth is representative of γ_h in the absence of Purcell enhancement. We employ $\beta_{\mathrm{wg}} = 32\%$, as derived from finite-difference time-domain (FDTD) simulations; $\eta_{DW} = 0.57$, from previous spectroscopic investigations [6]; and $\eta_{\mathrm{orb}} = 0.65$, from a fit to the integrated areas of the C and D peaks presented in Fig. 1(d) of the main text. Combining these estimates, we obtain a quantum efficiency of $\eta_{QE} > 51(8)\%$. We emphasize that this estimate represents a lower bound, as a nonideal separation between the emitter and the Bragg reflector would result in destructive interference, thereby lowering the fitted cooperativity and by extension the η_{QE} estimate.

To model the power dependence of the reflection contrast in Fig. 4c of the main text, we use the expression $\mathcal{R}(s) = \mathcal{R}(0)/(1+s)$ [14, 15], where $\mathcal{R}(0)$ is given by Eq. 6 and s is the saturation parameter.

[1] J. A. Martínez, R. A. Parker, K. C. Chen, C. M. Purser, L. Li, C. P. Michaels, A. M. Stramma, R. Debroux, I. B. Harris, M. H. Appel, *et al.*, Photonic indistinguishability of the tin-vacancy center in nanostructured diamond, Physical Review Letters **129**, 173603 (2022).

[2] L. Haber, R. Schaller, J. Johnson, and R. Saykally, Shape control of near-field probes using dynamic meniscus etching, Journal of Microscopy **214**, 27 (2004).

[3] M. J. Burek, C. Meuwly, R. E. Evans, M. K. Bhaskar, A. Sipahigil, S. Meesala, B. Machielse, D. D. Sukachev, C. T. Nguyen, J. L. Pacheco, *et al.*, Fiber-coupled diamond quantum nanophotonic interface, Physical Review Applied **8**, 024026 (2017).

[4] W. Wasserman, R. Harrison, G. Harris, A. Sawadsky, Y. Sfendla, W. Bowen, and C. Baker, Cryogenic and hermetically sealed packaging of photonic chips for optomechanics, Optics Express **30**, 30822 (2022).

[5] T. Iwasaki, Y. Miyamoto, T. Taniguchi, P. Siyushev, M. H. Metsch, F. Jelezko, and M. Hatano, Tin-vacancy quantum emitters in diamond, Physical Review Letters **119**, 253601 (2017).

[6] J. Görlitz, D. Herrmann, G. Thiering, P. Fuchs, M. Gandil, T. Iwasaki, T. Taniguchi, M. Kieschnick, J. Meijer, M. Hatano, *et al.*, Spectroscopic investigations of negatively charged tin-vacancy centres in diamond, New Journal of Physics **22**, 013048 (2020).

[7] J. Görlitz, D. Herrmann, P. Fuchs, T. Iwasaki, T. Taniguchi, D. Rogalla, D. Hardeman, P.-O. Colard, M. Markham, M. Hatano, *et al.*, Coherence of a charge stabilised tin-vacancy spin in diamond, npj Quantum Information **8**, 45 (2022).

[8] R. Debroux, C. P. Michaels, C. M. Purser, N. Wan, M. E. Trusheim, J. A. Martínez, R. A. Parker, A. M. Stramma, K. C.

Chen, L. de Santis, *et al.*, Quantum control of the tin-vacancy spin qubit in diamond, Physical Review X **11**, 041041 (2021).

[9] M. E. Trusheim, B. Pingault, N. H. Wan, M. Gündoğan, L. De Santis, R. Debroux, D. Gangloff, C. Purser, K. C. Chen, M. Walsh, *et al.*, Transform-limited photons from a coherent tin-vacancy spin in diamond, Physical Review Letters **124**, 023602 (2020).

[10] C. Hepp, T. Müller, V. Waselowski, J. N. Becker, B. Pingault, H. Sternschulte, D. Steinmüller-Nethl, A. Gali, J. R. Maze, M. Atatüre, *et al.*, Electronic structure of the silicon vacancy color center in diamond, Physical Review Letters **112**, 036405 (2014).

[11] J. Kim and H.-R. Noh, Analytical solutions of the second-order correlation function in resonance fluorescence for two-level systems, Journal of the Korean Physical Society **76**, 463 (2020).

[12] P.-J. Stas, Y. Q. Huan, B. Machielse, E. N. Knall, A. Suleymanzade, B. Pingault, M. Sutula, S. W. Ding, C. M. Knaut, D. R. Assumpcao, *et al.*, Robust multi-qubit quantum network node with integrated error detection, Science **378**, 557 (2022).

[13] A. Reiserer and G. Rempe, Cavity-based quantum networks with single atoms and optical photons, Reviews of Modern Physics **87**, 1379 (2015).

[14] A. Auffèves-Garnier, C. Simon, J.-M. Gérard, and J.-P. Poizat, Giant optical nonlinearity induced by a single two-level system interacting with a cavity in the purcell regime, Physical Review A **75**, 053823 (2007).

[15] A. Javadi, I. Söllner, M. Arcari, S. L. Hansen, L. Midolo, S. Mahmoodian, G. Kiršanskė, T. Pregnolato, E. Lee, J. Song, *et al.*, Single-photon non-linear optics with a quantum dot in a waveguide, Nature Communications **6**, 8655 (2015).